Supplementary Information

Tuning the Polarity of Dinitrile-Based Electrolyte Solutions for CO_2 Electro-reduction on Copper Catalysts

*Tatiana Morin Caamano[a], Mohamed S. E. Houache[b], Mario G. Sandoval[c], Martin Couillard[b], Arnaud Weck[c], Elena. A. Baranova[a], Yaser Abu-Lebdeh[b]**

[a] Department of Chemical and Biological Engineering, Center for Catalysis Research and Innovation (CCRI), University of Ottawa, Ottawa, Ontario K1N 6N5, Canada

[b] Energy, Mining and Environment Research Centre, National Research Council of Canada, Ottawa, Ontario K1A 0R6, Canada

[c] Department of Mechanical Engineering, Center for Research in Photonics, University of Ottawa, Ontario K1N 7N5, Canada

KEYWORDS: CO_2 electro-reduction, Nitrile-based organic electrolytes, CO_2 Solubility, Copper-based nanoparticles, Density functional theory.

Corresponding author:

Yaser Abu-Lebdeh - *National Research Council of Canada, Energy, Mining and Environment Ottawa, Ontario K1A 0R6, Canada;* orcid.org/0000-0001-8936-4238; Phone: +1 (613)949-4184; Email: Yaser.Abu-Lebdeh@cnrc-nrc.gc.ca; Fax: +1 (613)991-2384

Additional computational details

The Density Functional Theory (DFT) calculations were implemented by the Vienna Ab-initio Simulation Package (VASP).[1–3] The general gradient approximation (GGA) parametrized by the Perdew-Burke-Ernzerhof functional (PBE) was used as an exchange-correlation term.[4] The projector augmented wave (PAW) pseudopotential method was used to account for the electron-ion-core interaction.[5] For the plane-wave basis set, a cut-off energy of 520 eV was implemented. The molecules were optimized until the energy convergence was smaller than 10-5 meV and the forces acting on each atom were smaller than 10-3 eV/Å. Spin polarized calculations were considered, with the initial magnetic moment for each atom starting at zero. The van der Waals long-range order interactions phenomena, especially for the carbon-based molecules, were included in the computation as implemented by the DFT-D3 correction method of Grimme *et al.*[6] A gamma-centered 1x1x1 k-points mesh in the irreducible part of the Brillouin zone was used for reciprocal space integration for all calculated systems, following the Monkhorst-Pack scheme.[7] The ideal gas approximation was used for all molecules. Periodic boundary conditions were implemented in order to maintain a minimum distance of at least 13 Å of vacuum in between periodic images in all directions of each system, even when it interacts with a CO_2 molecule, to preclude interaction between interacting molecules and their images. To break the symmetry of the plane wave functions, unit cell parameters of 18.0x17.5x17.0 Å and 23.0x19.0x17.0 Å were considered for the acetonitrile and adiponitrile molecules cases, respectively, which was sufficient to prevent interactions between it and its periodic images as aforementioned. The interaction energy (E_{ads}) is calculated following the equation:

$$E_{ads} = E_{(M + CO_2)} - E_M - E_{CO_2}$$

where M refers to the host acetonitrile or adiponitrile molecules. $E_{(M+CO2)}$, E_M and E_{CO2} are the total energy of the M molecule interacting with the CO_2 molecule, the energy of the isolated M molecule and the energy of the isolated CO_2 molecule, respectively. The final configurations of modeled possible adsorption sites and their corresponding E_{ads} for all considered systems are presented in Table S4. Where for the ACN molecule, after CO_2 adsorption, four favorable positions surrounding de nitrile group (N-1 to -4) and four surrounding the methyl group (m-1 to -4), for the ADN molecule seven favorable position surrounding de nitrile group (N-1 to -7) and three surrounding the methylene group (m-1 to -3), and for the SEN molecule seven favorable position surrounding de nitrile group (N-1 to -7) and three surrounding the methylene group (m-1 to -2).

Electrochemical Cell Image

An image of the electrochemical cell is presented in Figure S1 below. Depicted on the left-hand side of the cell are the glassy carbon gas bubbler, glassy carbon working electrode, and not as apparent, the reference electrode, which was positioned behind the working electrode. On the right-hand side, resides the counter electrode, which consists of a Pt mesh electrode.

Figure S1. Image of assembled electrochemical cell.

Reference Electrode Calibration

Figure S2 displays the resulting ferrocene peak for glassy carbon in the acetonitrile electrolyte as reference for the electrode calibration process. The anodic and cathodic peak potentials occur at approximately 0.013 V and 0.130 V against the Ag/Ag^+ reference electrode respectively. Calculating the half wave potential ($E_{1/2}$) using $(E_{pa} + E_{pc})/2$ the obtained value was of 0.071 V vs Ag/Ag^+. The half wave potential then serves as a reference in order to be able to convert the measured potential against other types of reference electrodes. As such, utilizing the known $E_{1/2}$ of the Fc/Fc+ couple in acetonitrile is of 0.4 V vs NHE,[8] it can be seen that a shift of -0.329 V occurred. As such, to convert vs Ag/Ag^+ to NHE, the potential is to be shifted by +0.329 V for the conversion.

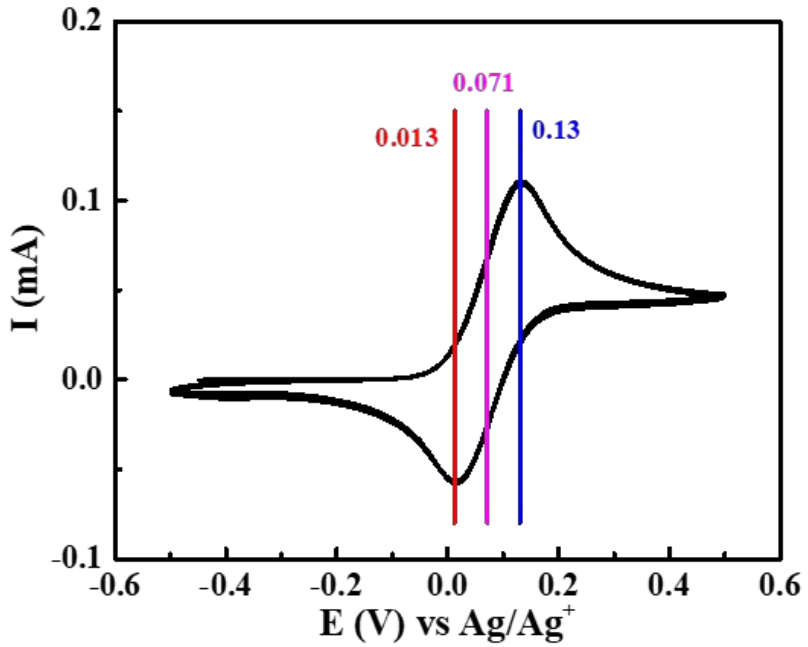

Figure S2. Ferrocene peaks for glassy carbon in 5mM ferrocene, 0.1M $TBAPF_6$ in acetonitrile.

FTIR Additional Data

The full FT-IR peak spectrum is provided in Figure S3 for all evaluated solvents along with water without CO_2 purge.

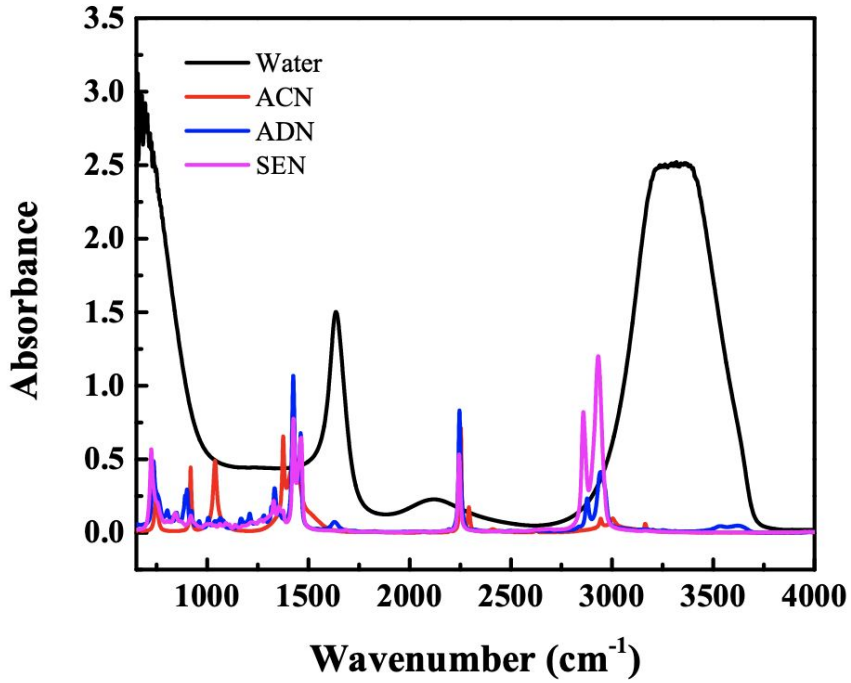

Figure S3. FT-IR peaks without CO_2 purge for water, acetonitrile, adiponitrile and sebaconitrile solvents.

Integration of the FT-IR CO_2 peaks was conducted using OriginPro@ software. The resulting integrated peaks from CO_2 saturation are shown in Figure S4. Meanwhile, the integrated peaks for the anhydrous ethanol reference are shown in Figure S5. Tabulated in Table S1 and Table S2 are the areas and the average areas with the standard deviation for the CO_2 peaks and ethanol peaks respectively. Table S3 displays the normalized area of the CO_2 peak over the ethanol reference peak areas, the CO_2 solubility from literature and calculated values, as well as the molar absorptivity. The molar absorptivity value was calculated from the known solubility values of water and acetonitrile. However, for adiponitrile and sebaconitrile the molar absorptivity was estimated to be close to that of acetonitrile. This was then used as a reference to estimate the CO_2 solubility for the two dinitrile solvents.

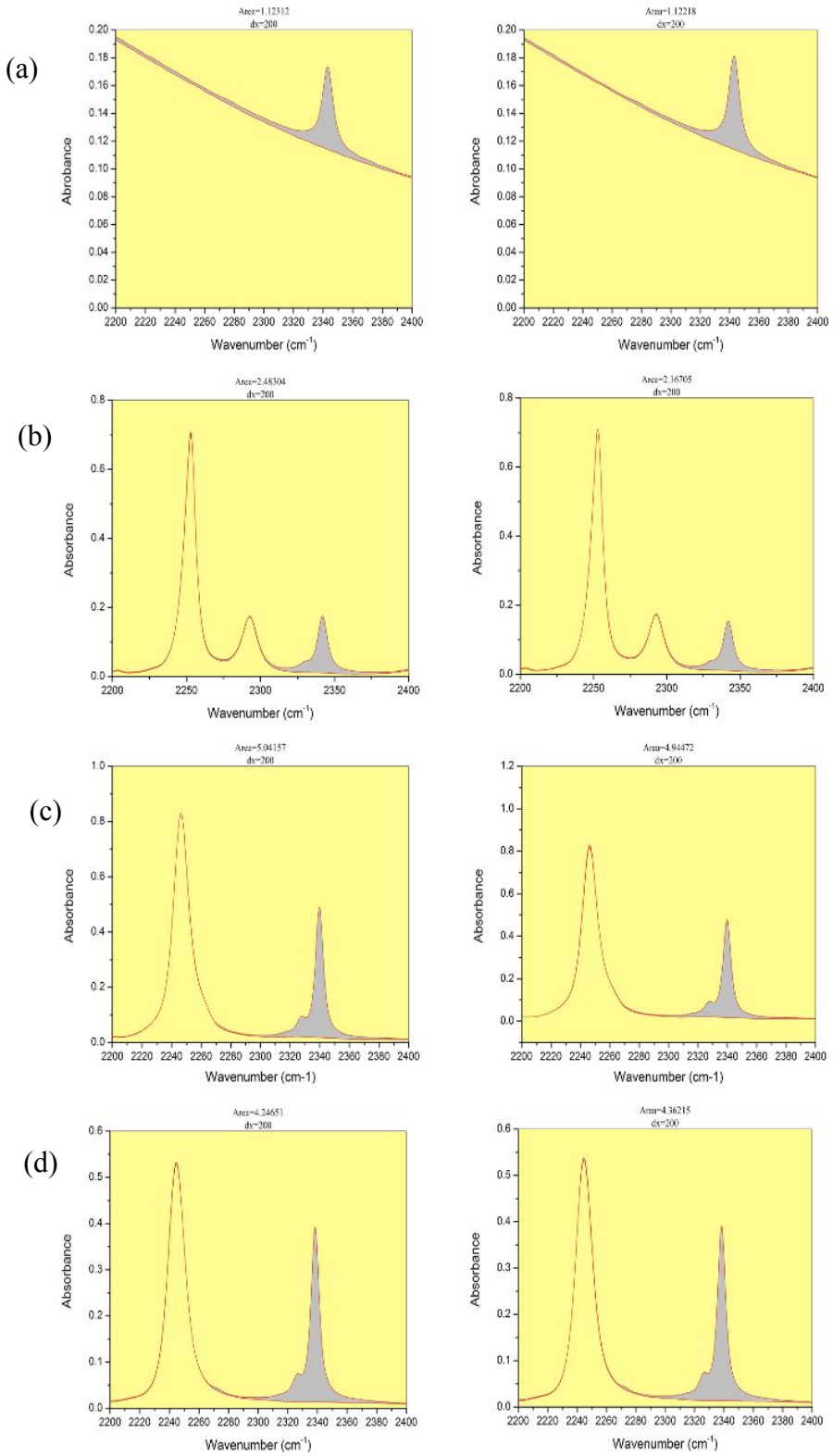

Figure S4. Integrated FT-IR CO_2 saturation peaks for (a) water, (b) acetonitrile, (c) adiponitrile and (d) sebaconitrile solvents.

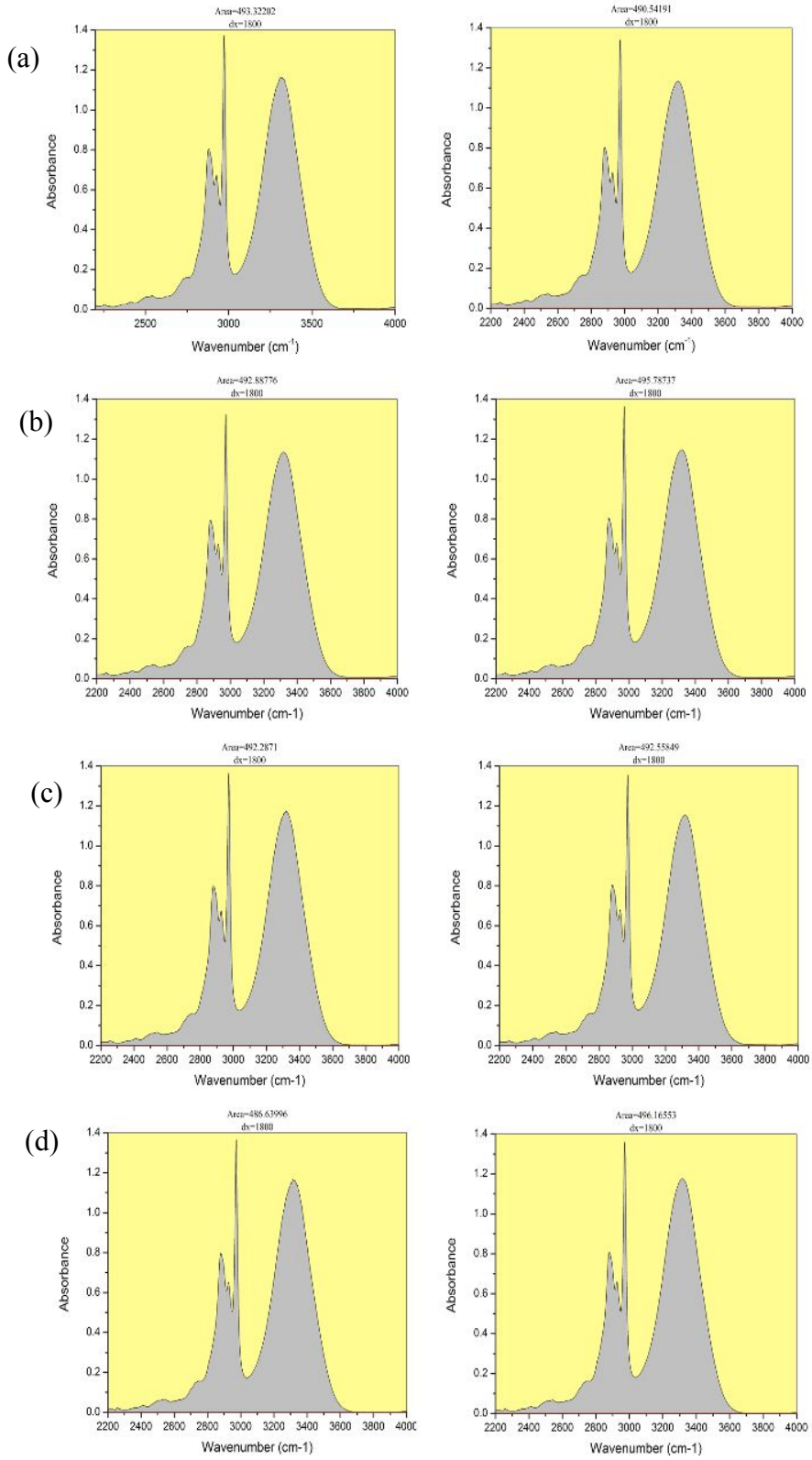

Figure S5. Integrated FT-IR anhydrous ethanol reference post-sampling (a) water, (b) acetonitrile, (c) adiponitrile and (d) sebaconitrile solvents.

Table S1. Resulting integrated and average areas from CO_2 peaks of FT-IR CO_2 saturated peaks.

	CO_2 Peak Area 1 (cm^{-1})	CO_2 Peak Area 2 (cm^{-1})	Average CO_2 Peak Area (μ, cm^{-1})	Standard Deviation (σ)
Water	1.12	1.12	1.12	0.001
Acetonitrile	2.48	2.17	2.33	0.223
Adiponitrile	5.04	4.94	4.99	0.068
Sebaconitrile	4.25	4.36	4.30	0.082

Table S2. Resulting integrated and average areas from anhydrous ethanol reference peaks of post-sampling FT-IR CO_2 saturated peaks.

	Ethanol Peak Area 1 (cm^{-1})	Ethanol Peak Area 2 (cm^{-1})	Average Ethanol Peak Area (μ, cm^{-1})	Standard Deviation (σ)
Water	493.3	490.5	491.9	1.97
Acetonitrile	492.9	495.8	494.3	2.05
Adiponitrile	492.3	492.6	492.4	0.19
Sebaconitrile	486.6	496.2	491.4	6.74

Table S3. Resulting Normalized CO_2 absorbance areas over ethanol reference areas, literature and estimated CO_2 solubility values, as well as calculated and estimated molar absorptivity values.

	Average CO_2 Peak Area (μ, cm^{-1})	Average Ethanol Peak Area (μ, cm^{-1})	Normalized CO_2 Absorbance Area (-)	CO_2 Solubility (mM)	Molar absorptivity (ε, L mol^{-1} cm^{-1})	
Water	1.12	491.9	0.002	40[9]	5.65E-06	Calc.
Acetonitrile	2.33	494.3	0.005	270[9]	1.72E-06	Calc.
Adiponitrile	4.99	492.4	0.010	582	1.72E-06	Est.
Sebaconitrile	4.30	491.4	0.009	503	1.72E-06	Est.

Calc. = molar absorptivity was calculated using Beer Lambert Formula, Est. = estimated molar absorptivity based on acetonitrile calculated value

Computational method: DFT

Table S4. The final configurations of the CO_2 adsorption over ACN, ADN and SEN molecules are listed. The adsorbate molecule specie, the adsorption site nomenclature and its lateral and frontal view, and the adsorption energy (E_{ads}) are shown from left to right columns, respectively.

Molecule	Adsorption site		E_{ads} (eV)
ACN	N-1		-0.126
	N-1		-0.119
	N-2	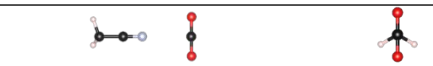	-0.119
	N-3	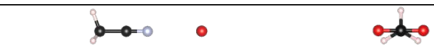	-0.119
	m-1	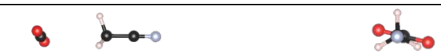	-0.041
	m-2		-0.041
	m-3		-0.041
	m-4		-0.041
ADN	N-1	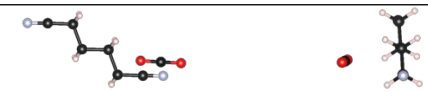	-0.145
	N-2	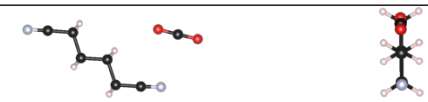	-0.142
	N-3	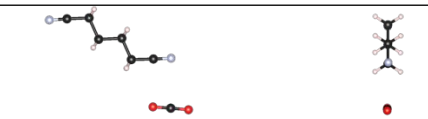	-0.121
	N-4	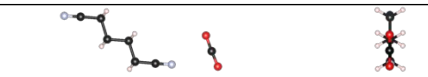	-0.117
	N-5		-0.115
	N-6	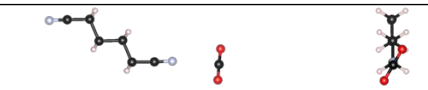	-0.114
	N-7		-0.114

	M-1		-0.116
	M-2	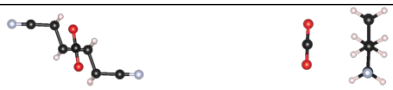	-0.105
	M-3		-0.096
SEN	N-1	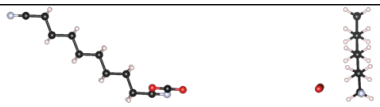	-0.141
	N-2	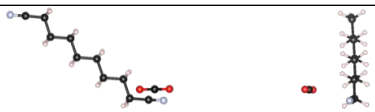	-0.139
	N-3	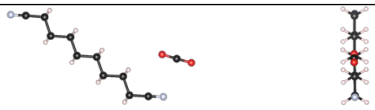	-0.137
	N-4	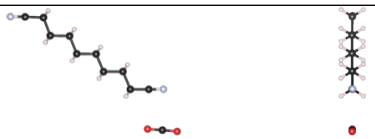	-0.121
	N-5	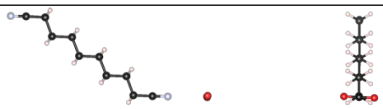	-0.119
	N-6	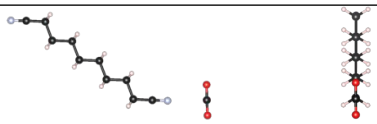	-0.119
	N-7	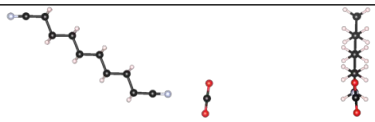	-0.118
	M-1	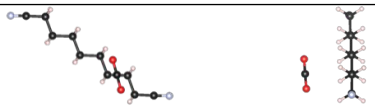	-0.112
	M-2	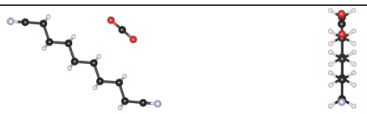	-0.097

Regarding electronic structure the Figure S6 showed the projected DOS curves for all considered systems before (dashed red line) and after (blue full line) CO_2 adsorption at the most stable site. Only the spin up contribution is plotted because all systems shown symmetric spin up and spin down contribution to the DOS curves. The CO_2-nitrile group interaction is present between the Fermi level and 6 eV, being the most important peaks around 6 eV (see Figures S6a-c). Also, in all cases the CO_2 molecule showed a shift to the lower energies.

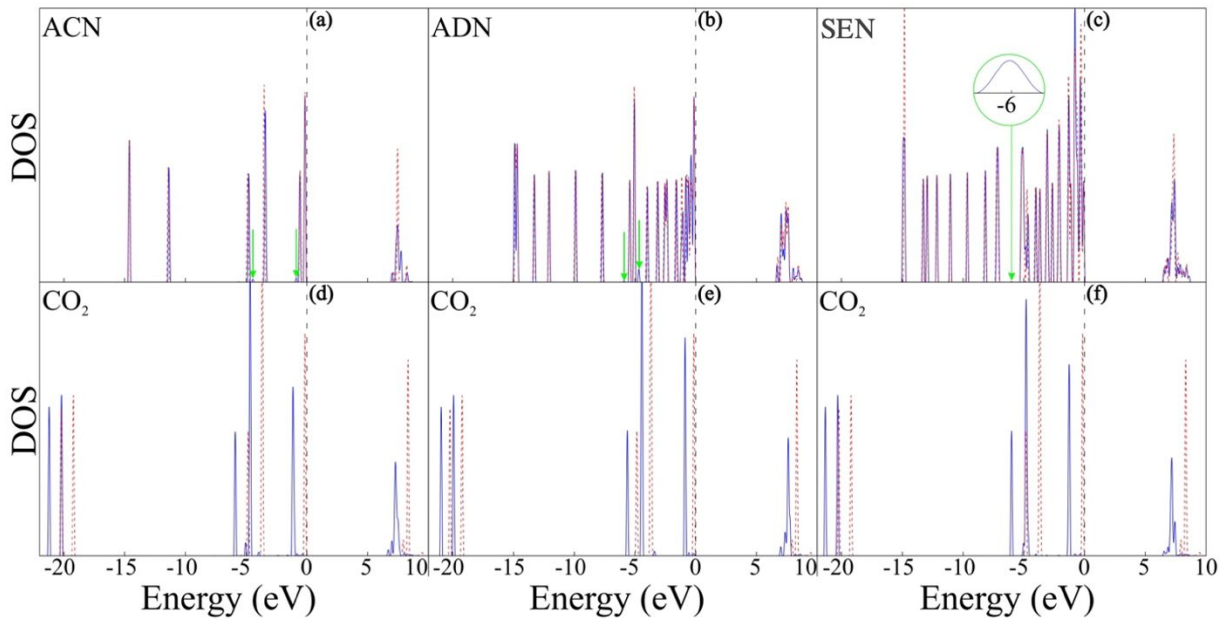

Figure S6. Projected DOS curves for ACN (a and d); ADN (b and e) and SEN (c and f) before (dashed red line) and after (blue full line) CO_2 adsorption at the most stable site. The green arrow indicates the CO_2-nitrile group interaction peaks. For a better view in the SEN case the interaction is showed magnified in the insert.

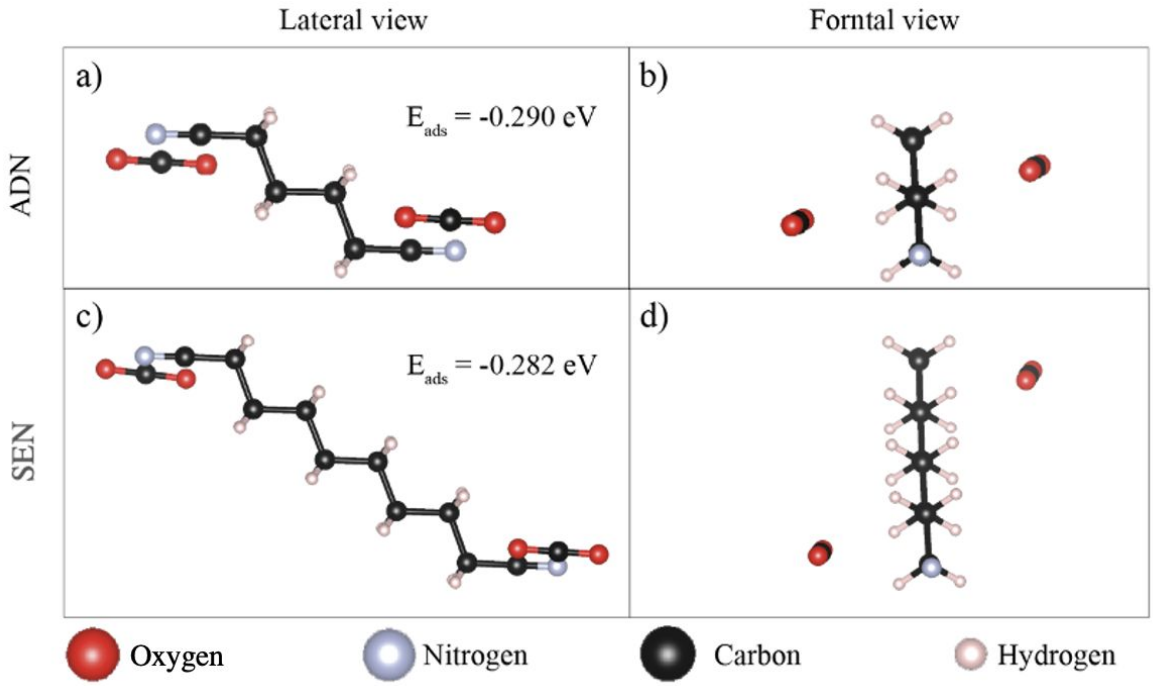

Figure S7. Lateral (left side) and frontal (right side) views of the final configuration of two CO_2 adsorbed at the opposite N-1 nitrile group sites for ADN and SEN (upper and lower subfigures).

Bader analysis as implemented by Tang *et al*.[12] was used to calculate electronic charges on atoms,[13] and the DDEC6 methodology was used to compute the net atomic charges (NACs) and bond order (BO) as described by Manz *et al.*[14–16] These calculations showed a weak interaction between the CO_2 and the nitrile-based molecules (see Table S5).

Table S5. Bond order (BO) for the CO_2-nitrile-based molecules after adsorption at the most stable adsorption site. The atomic labels correspond to those in Figure 3 in the main text.

Bond Type	ACN	ADN	SEN
C_1-O_A	0.019	0.017	0.019
N_1-O_A	0.011	0.008	0.009
N_1-C_A	0.021	0.019	0.022
N_1-O_B	0.010	0.010	0.011

Commercial Nanoparticle Characterizations

TEM images for the commercial copper particles are displayed in Figure S8. The commercial copper (Figure S8a), which was indicated to be 25 nm in TEM displayed this range in size. The CuO (Figure S8b), were expected to be of 40 nm in size based on manufacturer's indication. Based on the TEM images, the size are more uniform around the 40 nm range.

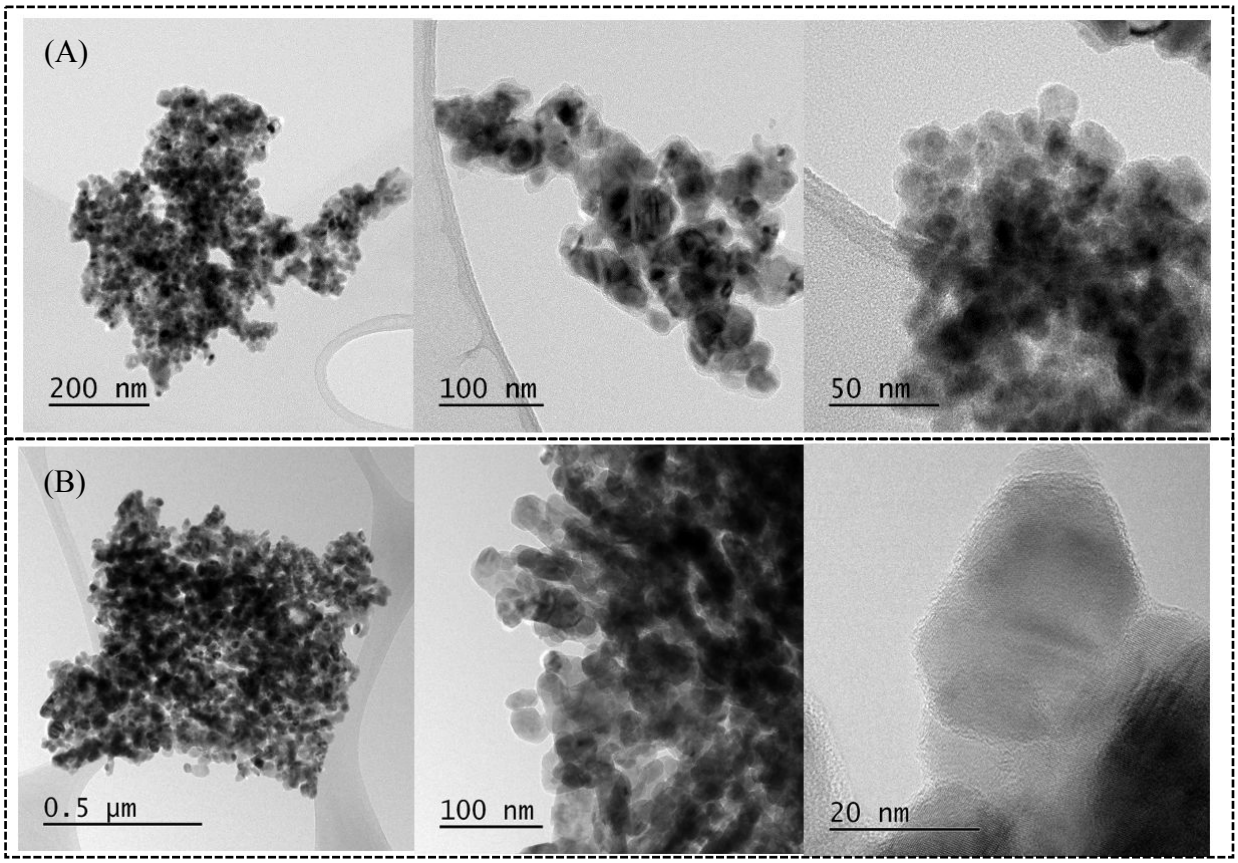

Figure S8. TEM images for (a) Cu and (b) CuO NPs catalysts.

XRD characterized peaks for the Cu commercial particles are displayed in Figure S9. The Cu commercial mainly shows significant diffraction peaks at 43.29°, 50.42° and 74.08° which align with the (111), (200) and (220) planes of the face centered cubic (fcc) structure of pure Cu (JCPDS no. 4-836).[10] Two smaller peaks were distinguished at 36.42° and 61.4°, which can be attributed to the (111) and (220) fcc structure planes of Cu_2O (JCPDS no. 5-667).[11] due to slight oxidation. Meanwhile the CuO commercial particles exhibit a monoclinic structure. The main 2θ peaks occurred at 35.46° and 38.72° attributed to the (-111) and (111) CuO structure planes (JCPDS no. 5-661).[11] Smaller peaks were also exhibited at 32.47°, 48.78°, 53.46°, 58.23°, 61.54°, 66.25°, 68°, 72.4° and 75.04°. These peaks could be attributed to the (110), (-202), (020), (202), (-113), (-311), (220), (311) and (-222) planes of CuO (JCPDS no. 5-661).[11] As such, it was confirmed that the main phases for each of the particle catalysts aligned well with their expected Cu and Cu oxide phases. The CuO nanoparticles exhibited no evidence of impurities, while the Cu particles displayed only slight evidence of Cu_2O oxidation beginning to form. The average crystallite sizes (D) estimated from the Debye-Scherrer formula were determined to be of 17.35 and 10.43 for the Cu and CuO commercial nanoparticles, respectively.

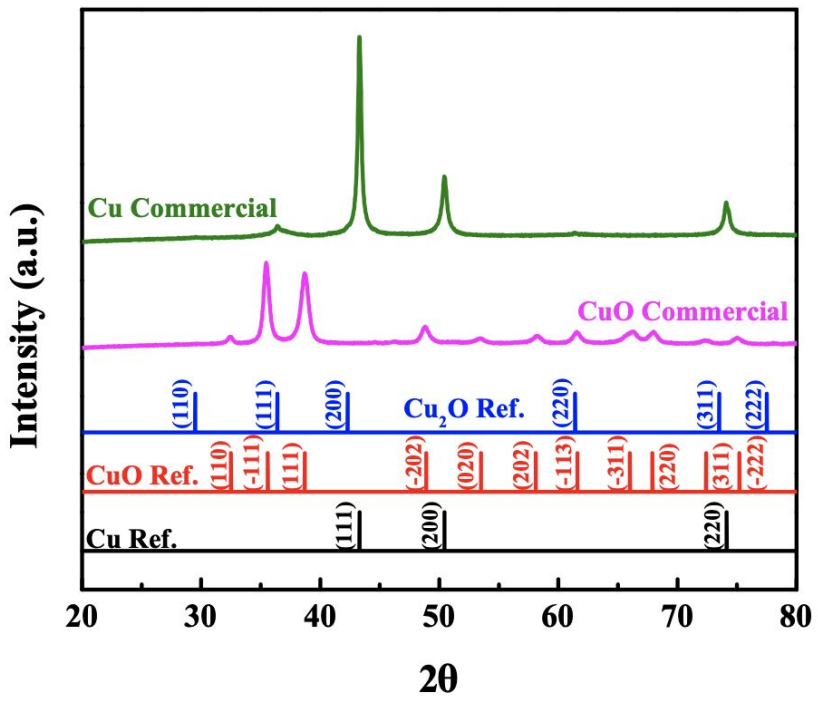

Figure S9. XRD Plots for Cu and CuO Commercial NPs.

Additional Electrochemical Analyses

Evaluations of electrochemical current densities for all organic electrolytes and a 0.1 M KHCO3 aqueous electrolytes under N_2 purge can be observed in Figures S10a and b. Figures S10c and d, depict enhanced CV curves of only the organic electrolytes. Additionally, the electrochemical current densities for all evaluated electrolytes under CO_2 purge for both catalysts can be observed in Figures S11a and b. Notably, a quantified comparison between the aqueous and organic electrolyte current densities cannot be made, as the potentials at which the reduction reactions occur are different.

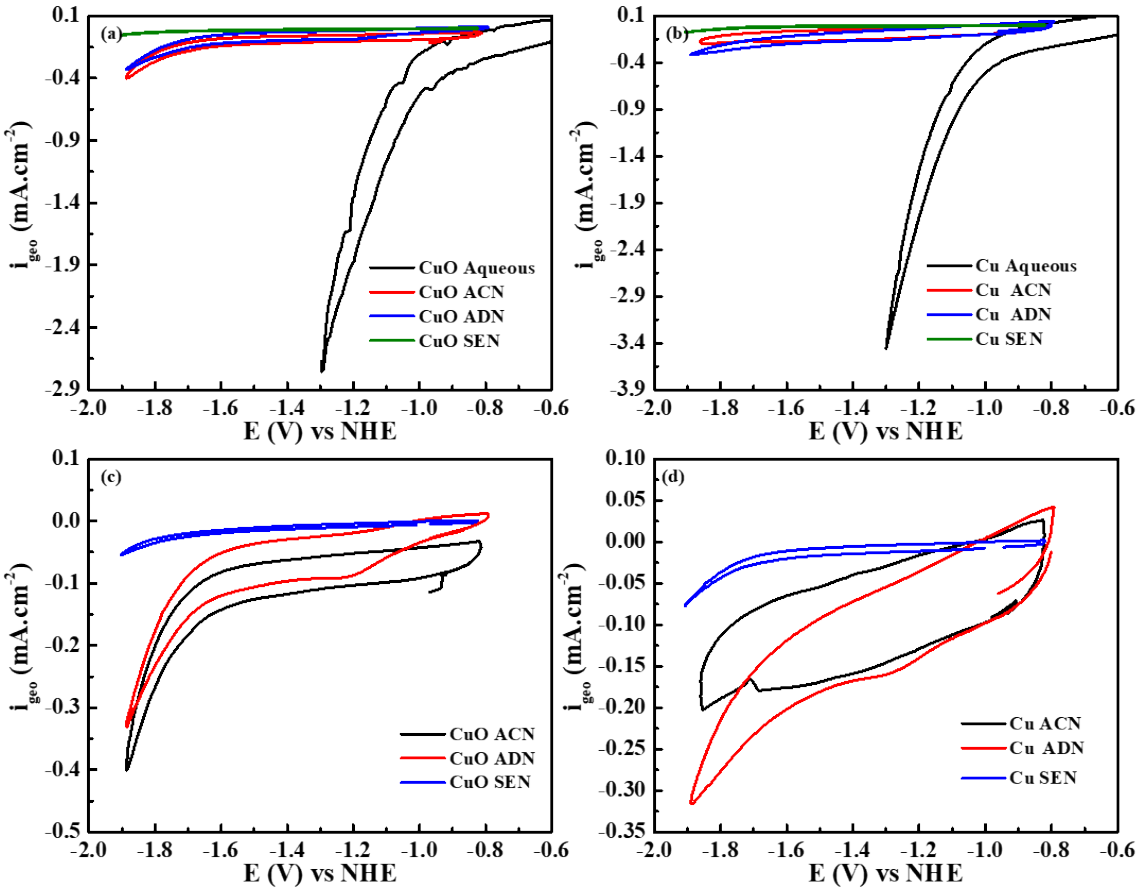

Figure S10. Cyclic Voltammograms of (a) CuO commercial and (b) Cu commercial in 0.1 M $KHCO_3$ aqueous, and 0.1 M $TBAPF_6$ acetonitrile, adiponitrile and sebaconitrile electrolytes. Enhanced (c) CuO commercial and Cu commercial in 0.1 M $TBAPF_6$ organic electrolytes at 50 mV.s^{-1} scan rate (fifth stable cycle).

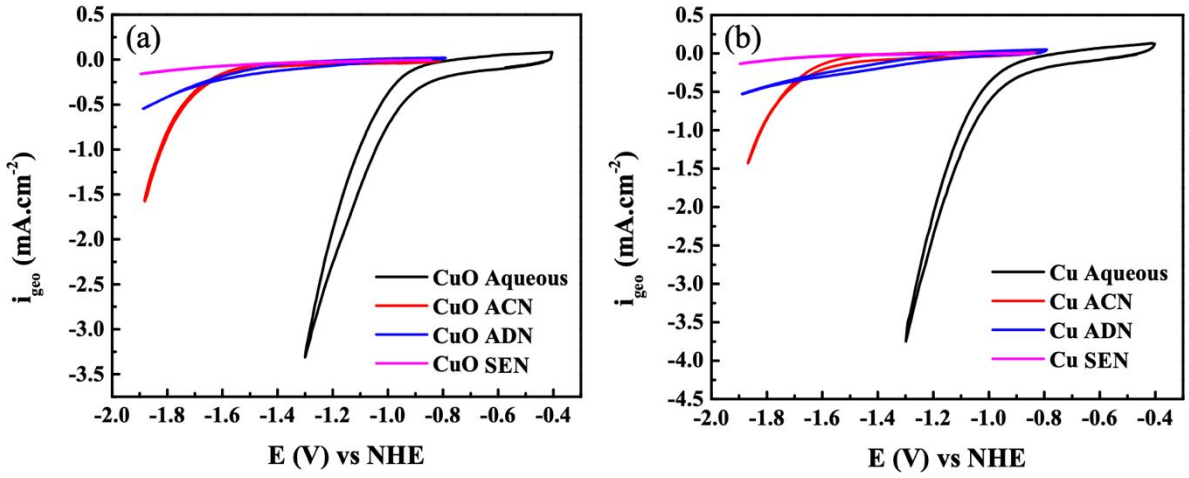

Figure S11. Cyclic Voltammograms of (a) CuO commercial and (b) Cu commercial in 0.1 M $KHCO_3$ aqueous, and 0.1 M $TBAPF_6$ acetonitrile, adiponitrile and sebaconitrile electrolytes at 50 mV.s^{-1} scan rate (fifth stable cycle).

To ensure that the decrease in activity from ACN to ADN was not a result of a required longer purging time in the electrochemical cell, a 3h CO_2 purge test in adiponitrile was also conducted. Seen in Figure S12 are both results for the 15 min purge and 3 h purge of CO_2 in ADN for a Cu catalyst. It can be observed that a difference of approximately 0.1 mA cm^{-2} can be observed. As such evidence for a lack of purging was not observed.

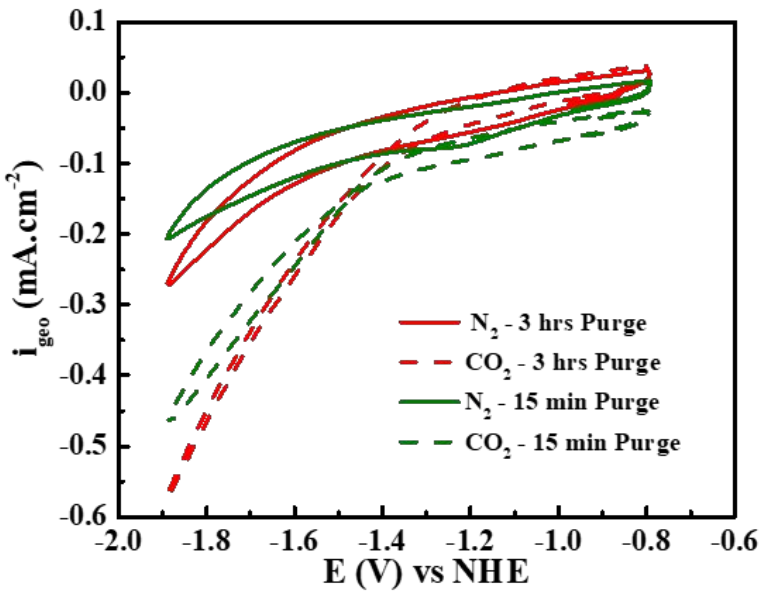

Figure S12. Cyclic Voltammogram of Cu in 0.1 M $TBAPF_6$ in adiponitrile with 3h CO_2 purge and 15min CO_2 purge at 50 mV.s^{-1} scan rate (fifth stable cycle).

Prior to CA measurements, CV under N_2 purge and CO_2 purge were conducted, and post-CA a CO_2 purge CV was also measured. Figure S13 shows the results of these tests for the ACN, ADN and SEN electrolytes for both tested catalysts. In line with CA results under ACN, the activity decreased after the CA with CuO commercial catalyst and increased with the Cu commercial catalyst. In ADN, results were again mirrored with increasing activity for CuO commercial and decreasing with Cu commercial. In SEN, although CA trends seemed relatively stable, a slight increase was seen in CuO commercial and a decrease with use of Cu commercial.

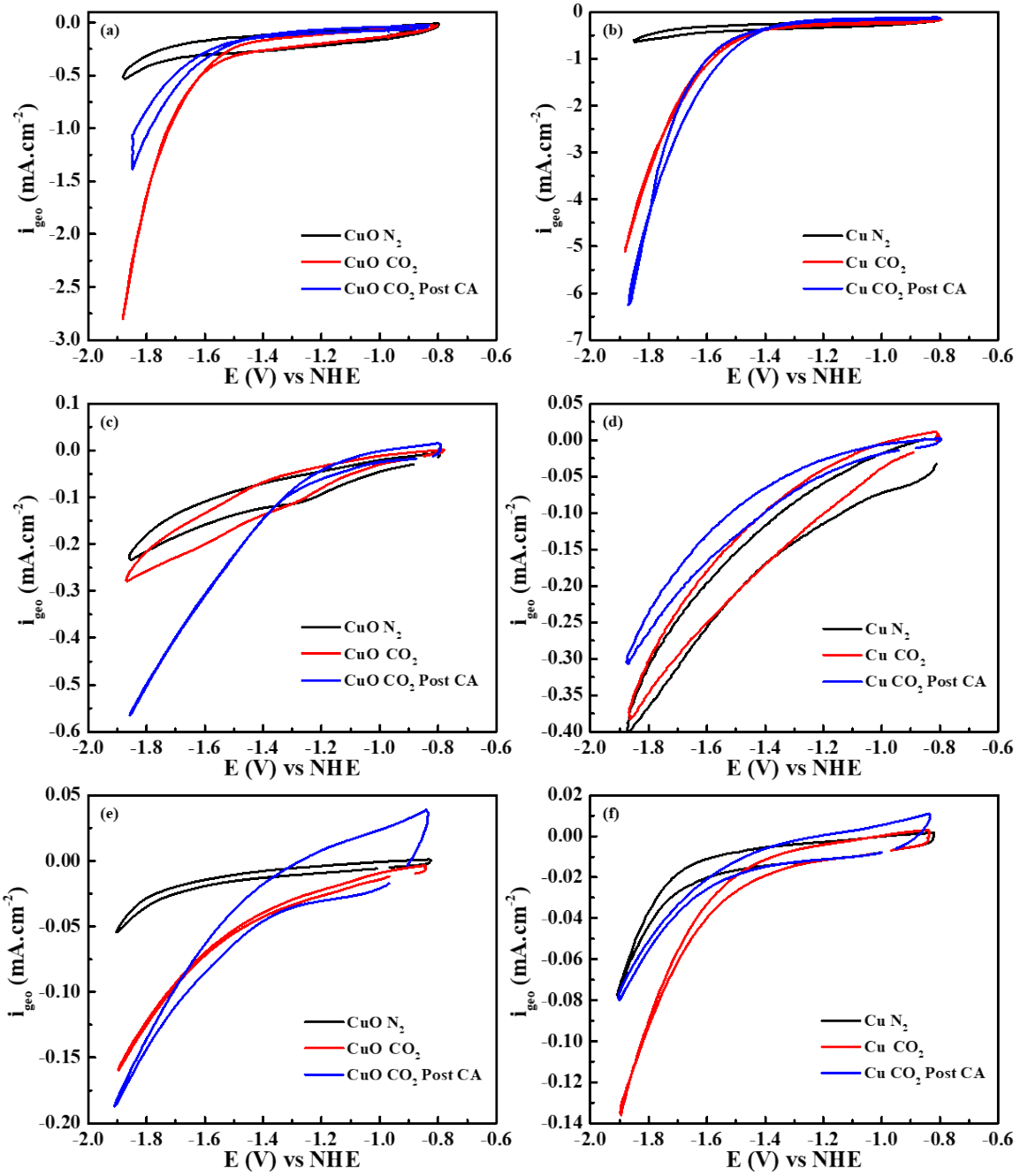

Figure S13. Cyclic voltammetry taken before and after CA experiments for (a,b) acetonitrile (c,d) adiponitrile and (e,f) sebaconitrile on both commercial CuO and Cu catalyst at 50 mV.s^{-1} scan rate (fifth stable cycle).

References

(1) Kresse, G.; Hafner, J. Ab Initio Molecular Dynamics for Liquid Metals. *Phys. Rev. B* **1993**, *47* (1), 558–561.

(2) Kresse, G.; Furthmüller, J. Efficiency of Ab-Initio Total Energy Calculations for Metals and Semiconductors Using a Plane-Wave Basis Set. *Comput. Mater. Sci.* **1996**, *6* (1), 15–50.

(3) Kresse, G.; Joubert, D. From Ultrasoft Pseudopotentials to the Projector Augmented-Wave Method. *Phys. Rev. B - Condens. Matter Mater. Phys.* **1999**, *59* (3), 1758–1775.

(4) Perdew, J. P.; Burke, K.; Ernzerhof, M. Generalized Gradient Approximation Made Simple. *Phys. Rev. Lett.* **1996**, *77* (18), 3865–3868.

(5) Blöchl, P. E. Projector Augmented-Wave Method. *Phys. Rev. B* **1994**, *50* (24), 17953–17979.

(6) Grimme, S.; Antony, J.; Ehrlich, S.; Krieg, H. A Consistent and Accurate Ab Initio Parametrization of Density Functional Dispersion Correction (DFT-D) for the 94 Elements H-Pu. *J. Chem. Phys.* **2010**, *132* (15).

(7) Monkhorst, H. J.; Pack, J. D. Special Points for Brillouin-Zone Integrations. *Phys. Rev. B* **1976**, *13* (12), 5188–5192.

(8) Pavlishchuk, V. V.; Addison, A. W. Conversion Constants for Redox Potentials Measured versus Different Reference Electrodes in Acetonitrile Solutions at 25°C. *Inorganica Chim. Acta* **2000**, *298* (1), 97–102.

(9) Moura de Salles Pupo, M.; Kortlever, R. Electrolyte Effects on the Electrochemical Reduction of CO_2. *ChemPhysChem* **2019**, *20* (22), 2926–2935.

(10) Theivansanthi, T.; Alagar, M. X-Ray Diffraction Studies of Copper Nanopowder. *Arch. Phys. Res.* **2010**, *1* (2), 112–117.

(11) Raghav, R.; Aggarwal, P.; Srivastava, S. Tailoring Oxides of Copper-Cu_2O and CuO Nanoparticles and Evaluation of Organic Dyes Degradation. *AIP Conf. Proc.* **2016**, *020078* (1724).

(12) Tang, W.; Sanville, E.; Henkelman, G. A Grid-Based Bader Analysis Algorithm without Lattice Bias. *J. Phys. Condens. Matter* **2009**, *21* (8).

(13) Bader, R. F. W. *Atoms in Molecules - A Quantum Theory*; Oxford University Press, 1990.

(14) Manz, T. A.; Limas, N. G. Introducing DDEC6 Atomic Population Analysis: Part 1. Charge Partitioning Theory and Methodology. *RSC Adv.* **2016**, *6* (53), 47771–47801.

(15) Limas, N. G.; Manz, T. A. Introducing DDEC6 Atomic Population Analysis: Part 2. Computed Results for a Wide Range of Periodic and Nonperiodic Materials. *RSC Adv.* **2016**, *6* (51), 45727–45747.

(16) Manz, T. A. Introducing DDEC6 Atomic Population Analysis: Part 3. Comprehensive Method to Compute Bond Orders. *RSC Adv.* **2017**, *7* (72), 45552–45581.